






Article

Pyrolytic Formation of TiO₂/Carbon Nanocomposite from Kraft Lignin: Characterization and Photoactivities

Dhanalakshmi Vadivel ^{1,2,*}, Diego Savio Branciforti ², Andrea Speltini ³, Michela Sturini ³, Vittorio Bellani ^{4,5}, Ilanchelian Malaichamy ^{1,*} and Daniele Dondi ^{2,5}

¹ Department of Chemistry, Bharathiar University, Coimbatore 641046, India

² Department of Chemistry and INFN, University of Pavia, via Taramelli 12, 27100 Pavia, Italy; diegosavio.branciforti@gmail.com (D.S.B.); daniele.dondi@unipv.it (D.D.)

³ Department of Drug Sciences, University of Pavia, via Taramelli 12, 27100 Pavia, Italy; andrea.speltini@unipv.it (A.S.); michela.sturini@unipv.it (M.S.)

⁴ Department of Physics, University of Pavia, via Bassi 6, 27100 Pavia, Italy; vittorio.bellani@unipv.it

⁵ Istituto Nazionale di Fisica Nucleare (INFN), University of Pavia, via Bassi 6, 27100 Pavia, Italy

* Correspondence: dhanalakshmi.vadivel@unipv.it (D.V.); chelian75@yahoo.com (I.M.)

Received: 10 February 2020; Accepted: 25 February 2020; Published: 1 March 2020



Abstract: This article reports on the formation of pyrolytic carbon/TiO₂ nanocomposite (p-C/TiO₂) by pyrolysis of a mixture of the P25 TiO₂ and kraft lignin at 600 °C. The result was characterized by X-ray diffraction (XRD), X-ray photoelectron spectroscopy (XPS), Raman spectroscopy, UV-visible spectroscopy, electron paramagnetic resonance spectrometry (EPR), thermogravimetry (TGA) and SEM microscopy. Its photocatalytic activity was ascertained using three classes of chemical probes, namely (i) degradation of methylene blue (MB) and rhodamine-B (RhB) dyes in UV light-irradiated aqueous suspensions, (ii) depletion of phenol and (iii) degradation of antibiotics. The p-C/TiO₂ nanocomposite is a strong physisorbent of both MB and RhB nearly twofold with respect to neat TiO₂. Although it is nearly twofold more photoactive toward the degradation of MB (0.091 min^{−1} versus 0.047 min^{−1}), it is not with regard to RhB degradation (0.064 min^{−1} versus 0.060 min^{−1}). For the degradation of phenol in aqueous media (pH 3), pristine TiO₂ was far more effective than p-C/TiO₂ for oxygenated suspensions (17.6 × 10^{−3} mM min^{−1} versus 4.3 × 10^{−3} mM min^{−1}). Under an argon atmosphere, the kinetics were otherwise identical. The activity of the material was tested also for a real application in the degradation of a fluoroquinolone antibiotic such as enrofloxacin (ENR) in tap water. It is evident that the photoactivity of a semiconductor photocatalyst is not a constant, but it does depend on the nature of the substrate used and on the experimental conditions. It is also argued that the use of dyes to assess photocatalytic activities when suspensions are subjected to visible light irradiation is to be discouraged as the dyes act as electron transfer photosensitizers and or can undergo photodegradation from their excited states.

Keywords: kraft lignin; pyrolytic carbon; nanocomposite; dyes photodegradation; phenol; fluoroquinolone; photocatalytic activity

1. Introduction

Titanium dioxide (TiO₂) is the most valuable semiconductor material used widely in many fields that include photochromics, pigments, solar energy conversion devices, sensors and, within the present context, as a photocatalyst able to decay organic contaminants in aquatic and air environments [1–5]. It has been examined and used extensively because of its high photoactivity, long-term stability, low toxicity, ecofriendly characteristics and relatively low cost. Nonetheless, TiO₂ does present some disadvantages that significantly restrict many of its practical applications that use sunlight such as,

for example, rapid recombination of photogenerated electron–hole pairs (lifetime about 30 ns) [6] when irradiated with UV light and its low efficiency in the utilization of solar light (absorption edge for rutile: 400 nm; for anatase: 387 nm). Consequently, reducing or suppressing the recombination of charge carriers is essential for the improvement of titania's photoactivity.

A variety of strategies have been proposed and used in the past decade to increase the efficiency of TiO₂-based photocatalysts; for instance, a more crystalline and suitable textural design, doping this metal oxide with noble metals and/or with non-metals or else forming suitable nanocomposites with other semiconductors to produce second- and third-generation photocatalysts [7–10]. Therefore, the use of favorable conductive substrates to overcome some of the barriers to practical applications is of utmost importance. Composite materials of TiO₂ with various carbonaceous materials, such as hollow carbon microspheres and carbon nanotubes, have demonstrated good conductivity and strong absorption of light [11,12], which have contributed significantly to the effective photodegradation of environmental pollutants [13]. Currently, there is growing interest in the combination of graphene-based materials with TiO₂ to enhance the photocatalytic performance of the latter [14–18].

Kraft lignin is an abundant natural raw material (50 million tons per year) generally obtained from black liquor discharged from paper mills that poses major disposal problems. Much of the so-produced lignin is consumed as a fuel, in addition to some other marginal applications as an adhesive or as a tanning agent. It is an integral part of lignocellulosic materials with quantities that vary from 10% to 30%. Other lignocellulosic materials that are sources of lignin include agricultural residues, plant substrates and cork. Within the present context, an interesting application of kraft lignin is as a precursor to produce activated carbons (ACs) that have proven useful as adsorbents [19]. Indeed, the use of lignin as a precursor to produce ACs has been shown to be an interesting alternative to incineration. ACs have been synthesized by physical activation and by chemical activation. In the latter case, chemical activation of kraft lignin with ZnCl₂ at temperatures 400–500 °C produces high-surface-area ACs with a predominantly microporous structure. However, environmental issues with ZnCl₂ to activate lignin have led to the use of ortho-phosphoric acid as the preferred activating/dehydrating agent [20].

A new nanomaterial composed of ultra-small TiO₂ nanoparticles and reduced graphene oxide (rGO) nanosheets was reported by Gu and coworkers [21] who used glucosamine as the carbon source in alkaline media through a hydrothermal treatment; the 13-nm TiO₂ nanoparticles were strongly anchored on the graphene structure. The TiO₂/rGO obtained through a thermal treatment at 700 °C exhibited better photoactivity in the photodegradation of methyl orange than those produced at other calcination temperatures; it also displayed good photoactivity toward the degradation of rhodamine-B (RhB) and methylene blue (MB). Along similar lines, Sun et al. [22] synthesized TiO₂/graphene nanorods via a one-step hydrothermal method that featured the concomitant reduction of graphene oxide (GO). XPS results revealed the formation of Ti–C bonds between the TiO₂ and graphene while Raman spectral results demonstrated the reduction of GO to graphene in the as-prepared nanocomposites, which also showed a red shift in the optical absorption edge and enhanced absorbance of the TiO₂/graphene nanorods compared to bare TiO₂ nanorods. The nanocomposites displayed greater photoactivity than naked TiO₂ nanorods toward the photodegradation of MB under visible light irradiation; however, this is not surprising as the MB dye becomes a photosensitizer of the TiO₂ through electron injection under the irradiation conditions used [23]. Regardless, the authors [22] attributed this enhanced photoactivity to (i) improved adsorption of the dye on the composite nanorods, (ii) extended light absorption with greater wt.% of graphene and (iii) more efficient charge transport and electron–hole separation. Dong et al. [24] used a one-step solvothermal method to produce graphene/rod-shaped TiO₂ nanocomposites with improved photocatalytic activity.

A review by Giovannetti and coworkers [25] summarized the extensive literature on graphene-based titania nanocomposites and their photocatalytic applications toward the oxidative decomposition of synthetic dyes. Both graphene (G) and graphene oxide (GO) have been used to synthesize a series of TiO₂/GO and TiO₂/G hybrid materials employing various methods; their

corresponding photoactivities have also been the subject of extensive investigations, particularly with graphene oxide [26,27] and graphene sheets with facets of anatase TiO_2 [28]. For instance, Zhang and coworkers [29] reported a photocatalyst, chemically bonded TiO_2 (P25)-graphene nanocomposite by a simplistic one-step hydrothermal method, which led to reduction of the graphene oxide loaded onto P25 titania. The as-prepared P25/graphene system displayed great adsorption of the MB dye as well as extended light absorption into the visible spectral region; the intrinsic bandgap of P25 TiO_2 was 3.1 eV while the extrinsic bandgap of the TiO_2 /graphene system was 2.82–2.88 eV. From the data reported by Zhang et al. [29], UV irradiation of the MB with TiO_2 and TiO_2 /G suspensions under ambient atmospheric conditions led to approximately 6% and 65% of the adsorbed MB to decompose, respectively, after less than 1 h. Du and coworkers [30] succeeded in incorporating graphene into macro-mesoporous titania frameworks through in situ reduction of graphene oxide, which resulted in improved mass transport via the film, reduced length of the mesopore channel and increased accessibility of the surface area of the thin film, while effectively suppressing charge recombination in TiO_2 that led to significant enhancement of the photocatalytic activity in degrading the MB dye. The reported apparent rate constants for the degradation on these macro-mesoporous titania films with and without graphene were 0.071 min^{-1} and 0.045 min^{-1} , respectively.

Wang et al. [31] examined commercial anatase TiO_2 , graphene-on- TiO_2 (G/ TiO_2) and TiO_2 -on-graphene (TiO_2 /G) composites, the latter two being synthesized by a combination of a simple sol-gel self-assembly method and a thermal annealing process. Under UV light illumination, the photocatalytic activity of the G/ TiO_2 composite toward the degradation of rhodamine 6 G was greater than that of TiO_2 as a result of three factors: (a) graphene is a viable acceptor material because of its π -conjugated structure in two-dimensional, (b) its two-dimensional planar structure gives it with unexpectedly good conductivity due to benefits the transport of charge carriers and (c) the photocatalytic performance of G/ TiO_2 is based on the preparation methods. Moreover, the enhancement of photoactivity of G/ TiO_2 nanocomposites was ascribed to the incorporation of C contents into the matrix of TiO_2 that increases the absorptivity and the life span of photoexcited e^-/h^+ pairs [31]. Mechanistically, they inferred that in the presence of graphene, with a π -conjugated structure, the photogenerated electrons are transferred from the CB of TiO_2 to the surface of graphene then react with oxygen to produce reactive oxygen species such as HO_2^\bullet , $\text{O}_2^{\bullet-}$ and $\bullet\text{OH}$, with the holes left in the VB of TiO_2 being transferred to the surface and oxidize directly the adsorbed dye molecules, as well as reacting with water to produce additional $\bullet\text{OH}$ radicals. On the other hand, Posa and coworkers [32] prepared TiO_2 -graphene nanocomposites (nanosheets of graphene) by an easy chemical method by using graphene oxide and titanium isopropoxide as precursors. An examination of the photocatalytic activity of the nanocomposite in the degradation of RhB in aqueous media under solar light irradiation for 60 min revealed a removal of 98% as compared with pure TiO_2 (42%), graphite oxide (19%) and a mechanical mixture of graphene and TiO_2 (60%) owing to increased light absorption and reduced electron-hole pair recombination upon intercalation of graphene and TiO_2 .

A wide-ranging work enclosing a computational study focused on the titania-graphene (TiO_2 /G) nanocomposite interface and on its photocatalytic performance on MB degradation using different quantities of G on P25 TiO_2 has been carried out by Martins et al. [33]. Experimental results revealed that the nanocomposite TiO_2 /G (3.0% in graphene) degraded MB more efficiently (0.160 min^{-1}) than TiO_2 alone (0.070 min^{-1}). Computational results showed that the nanocomposites are potentially more efficient than pure TiO_2 because of their lower experimental bandgaps (2.94 to 2.75 eV versus 3.08 eV for TiO_2) and to charge separation at the interfaces that reduces recombination of electron-hole pairs. For their part, Zhang and coworkers [34] reported a unique route for the synthesis of graphene/ TiO_2 continuous fibers by using force spinning combined by water vapor annealing method. The incorporation of graphene in TiO_2 fibers enabled lowering the bandgap and improve the photo-induced charge separation in the photocatalyst. As a result of synergistic effects, 2 wt.% of graphene on TiO_2 fibers proved the highest photocatalytic activities in the degradation of reactive brilliant red X-3B textile dye under UV irradiation, far superior to the photocatalyst P25 titania.

Mechanistically, the authors [34] proposed that electrons were largely trapped by defect sites (e.g., as Ti^{3+} and oxygen vacancies) or efficiently transferred from the conduction band of TiO_2 to graphene prior to recombination, as evidenced by XPS in that a C-Ti covalent bond was formed between TiO_2 and graphene that facilitated the charge transfer, resulting in a lower recombination degree of carriers and enhanced photoactivity.

Herein, we report the formation of pyrolytic carbon supported onto TiO_2 nanoparticles (p-C/ TiO_2) by high-vacuum pyrolysis of kraft lignin as the pyrolytic carbon source at 600 °C in the presence of the well-known commercially available P 25 TiO_2 . The resultant material was characterized by Raman spectroscopy, electron paramagnetic resonance (EPR) spectrometry, thermogravimetry (TGA), scanning electron microscopy (SEM), UV-visible and X-ray photoelectron spectroscopy (XPS). Results demonstrated unambiguously that the resulting material was a combination of carbon and TiO_2 . Its photoactivity was assessed and compared to pristine TiO_2 using three different classes of chemical probes: (i) degradation of MB and RhB dyes in UV light-irradiated suspensions with the course of the oxidative process monitored by UV-visible absorption spectroscopy; (ii) depletion of phenol in suspensions irradiated by a UV-visible light source in the absence and presence of oxygen; and (iii) degradation of a fluoroquinolone antibiotic under simulated solar light monitored by high-performance liquid chromatography with UV detection (HPLC–UV). The novelty of the work is that the carbon/ TiO_2 photocatalyst was prepared from cheap waste materials like kraft lignin without the use of solvents or chemicals. This is possible by the high-vacuum pyrolysis technique used in this work. In this regard, we approach the synthesis of the catalysts in a Green Chemistry way to maintain the circular economy perspective. Moreover, pyrolytic carbon increases the adsorption of chemicals before irradiation, rendering the material useful for a preconcentration of pollutants from waters and then cleaning of the catalyst after irradiation.

2. Results and Discussion

2.1. Pyrolysis and Materials Characterization

2.1.1. X-ray Powder Patterns

Evonik P25 titania is a nanosized photocatalyst consisting of the anatase and rutile polymorphs, together with some amorphous phase. Kraft lignin was selected as the carbon source since its pyrolysis produces pyrolytic carbonaceous residues [35,36]. Taking into account that above a pyrolysis temperature of 600 °C the fraction of the anatase phase in P25 TiO_2 is converted into rutile, all pyrolysis experiments were carried out at or below this temperature so as not to influence the photocatalytic activity of this metal oxide, as rutile TiO_2 is well-known to be less photoactive than anatase TiO_2 .

X-ray diffraction patterns of pristine TiO_2 , p-C/ TiO_2 before and after the pyrolysis clearly demonstrate that no phase change occurred during the pyrolytic process. Moreover, the XRD results also show that the p-C/ TiO_2 after the pyrolysis is not graphene oxide as the latter displays a peak signal at $2\theta = 10.2^\circ$ [37] which is clearly missing in the XRD patterns of Figure 1.

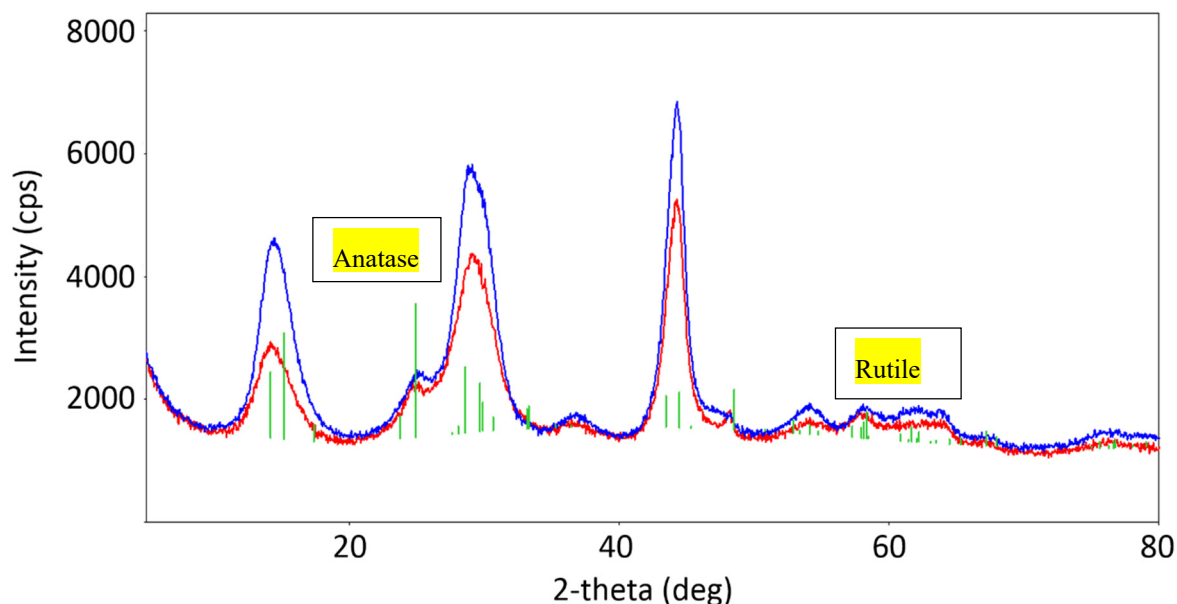


Figure 1. XRD patterns of pristine TiO_2 (red) and pyrolytic carbon/ TiO_2 nanocomposite (p-C/ TiO_2) (blue) specimens. The green lines refer to the diffraction peaks of titania available in the instrument's database.

2.1.2. X-ray Photoelectron Spectroscopy (XPS)

The nature of the material was further investigated by XPS. As expected, there was no significant carbon presence on pristine titania except for a small peak attributed to C_{1s} due to adsorbed carbon dioxide from the air (Figure 2a). By contrast, in the p-C/ TiO_2 sample, in addition to the Ti_{2p} and O_{1s} (Figure 2a), there appears strong, clearly visible carbon-related signals (Figure 2b) attributable to the binding energy of carbon–carbon and carbon–hydrogen bonds at ca. 285 eV; some weak signals of oxygenated carbons also appear on the pyrolyzed material at 286.6 and 288.9 eV. In the present instance, however, the graphenic zone at ca. 285 eV is far more predominant consistent with previous results [37].

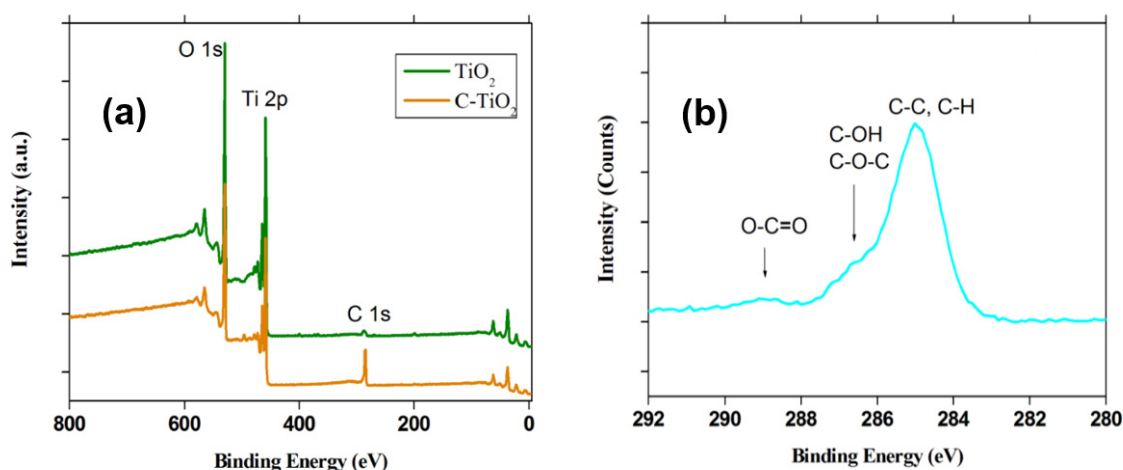


Figure 2. (a) XPS of pristine TiO_2 (green curve) and p-C/ TiO_2 (brownish curve) samples; (b) expansion of the carbon-related region of interest for the p-C/ TiO_2 sample.

2.1.3. Raman Spectral Analysis

Raman spectra of pristine P25 TiO_2 and the p-C/ TiO_2 are displayed in Figure 3, which confirm that no anatase to rutile phase change occurred as evidenced by the three titania Raman peaks in the range $300\text{--}800\text{ cm}^{-1}$ after the kraft lignin/ TiO_2 mixture had been subjected to the $600\text{ }^\circ\text{C}$ pyrolysis.

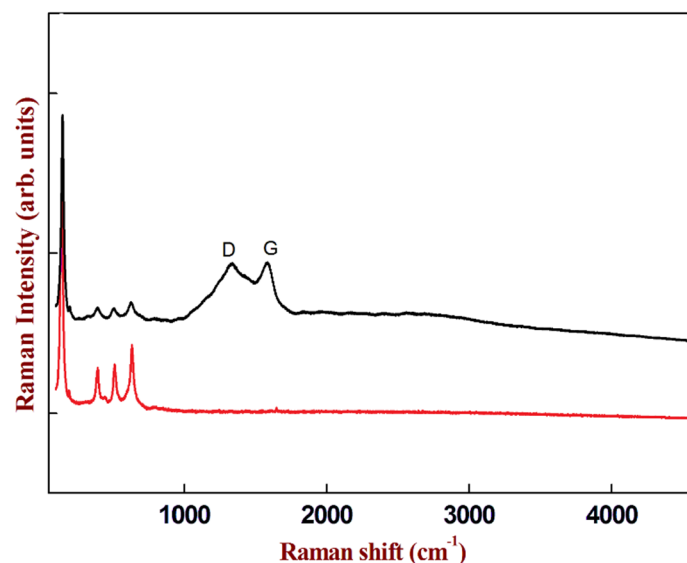


Figure 3. Raman spectra of the p-C/TiO₂ specimen prepared at a temperature of 600 °C (black curve) and of pristine (neat) P25 TiO₂ (red curve).

Unlike the Raman spectrum of neat TiO₂ (curve 2), the corresponding Raman spectrum of the p-C/TiO₂ sample (curve 1) displayed a clear G band at 1580 cm^{−1} originating from the stretching mode of *sp*²-type C–C covalent bonds; a D band was also present at 1320 cm^{−1}, indicating a highly defective carbon material owing to an increase of the *p* character of carbon. This is in accordance with the work of Sun et al. [22] who noted that the D band provides information on *sp*³ defects in carbon, while the G band is a common feature for in-plane vibrations of *sp*² bonded carbons. Moreover, the relative intensity of the D band to the G band usually indicates the order of defects in carbon materials.

The defective nature of the resulting p-C/TiO₂ material presents some advantages in view of its facile chemical functionalization, which relies mainly on the presence of radicals. The carbonaceous part of the p-C/TiO₂ nanocomposite can also act as an efficient chemical adsorbent of environmental contaminants such as, for example, dyes and aromatics.

2.1.4. Electron Paramagnetic Resonance Spectroscopy

The nature of the residual pyrolytic carbon on titania was also assessed by EPR spectroscopy. The relevant spectrum of p-C/TiO₂ measured at ambient temperature shows a singlet (Figure 4) at about 3350 gauss (*g* factor = 2.0026; Cr³⁺ was the internal reference for the calculation of the *g* factor) that is clearly attributable to a carbon-centered radical. Neat TiO₂ (that was also subjected to pyrolytic conditions identical to those of p-C/TiO₂ samples) displayed no detectable EPR signals. Evidently, the pyrolytic carbon residue formed stabilized radicals subsequent to the pyrolysis of the TiO₂/lignin system. Not unrelated to the present study, Lyon and coworkers [38] investigated electron spin resonance in a monolayer of graphene on a Si/SiO₂ substrate in which the *g* factor was 1.952 ± 0.002 and insensitive to charge carrier type, concentration and mobility. A recent study by Panich et al. [39] attributed the EPR signal in graphenes as originating either from the π -electronic edge-localized spins interacting with molecular oxygen, or to some stable defects in graphene that are insensitive to the oxygen environment. In our present case, the obtained *g* factor value is more relevant to stable carbon radicals produced by defects in p-C/TiO₂.

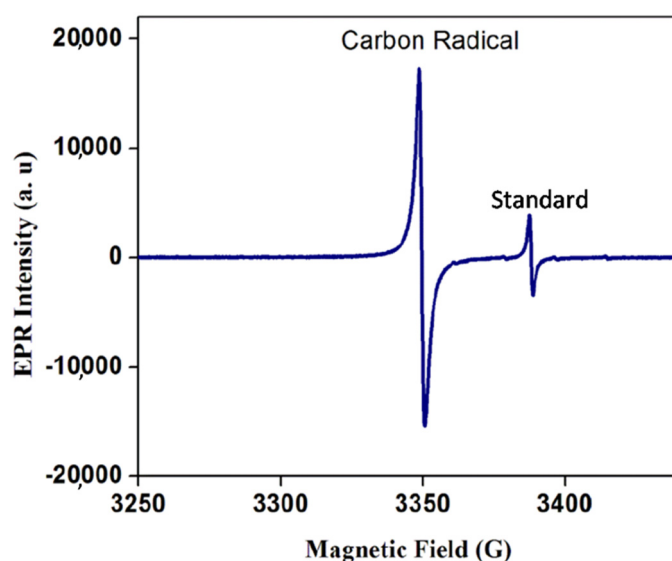


Figure 4. Spectrum of the p-C/TiO₂ system; Cr⁺³ was the internal standard.

2.1.5. UV-Visible Absorption Spectroscopy

Figure 5 shows the UV-visible absorption spectra of p-C/TiO₂ with TiO₂ reference. They revealed an absorption peak at 320 nm with differential spectral change. The optical bandgap energies are calculated as 3.16 eV for and 2.63 eV for, respectively, titania and p-C/TiO₂ obtained by using the Tauc plot. The value 2.63 eV is very close to important allotropes like graphene thin layer supporting the nature of carbon present on the catalyst [40].

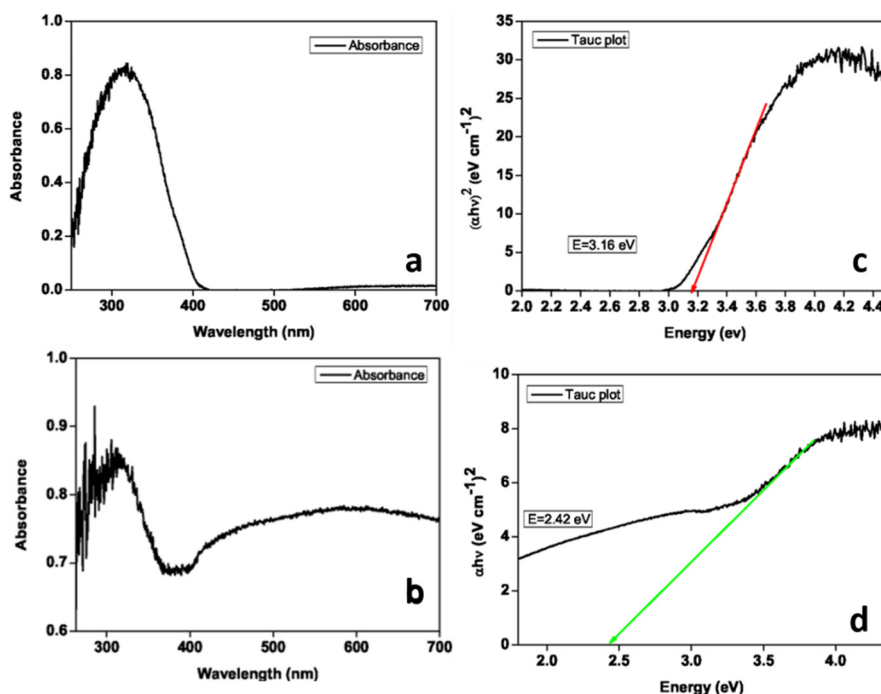


Figure 5. (a,b) UV-visible absorption spectra of TiO₂ and p-C/TiO₂. (c,d) Tauc plot of TiO₂ and p-C/TiO₂ to find the bandgap, respectively.

2.1.6. Thermogravimetric Analysis

The thermogravimetric analysis (TGA) performed on the p-C/TiO₂ sample as a function of temperature and time under a nitrogen atmosphere and under air revealed a loss of ca. 1.5 wt.% related

to moisture and about 2.8 wt.% carbon, inferring a relatively stable carbon-supported TiO_2 system as p-C/ TiO_2 .

2.1.7. Scanning Electron Microscopic Analysis

Figure 6a–c shows the SEM images of pristine TiO_2 , p-C/ TiO_2 and representative measured sizes of the nanocomposite particles (scale bar 200 nm), respectively, that appear highly agglomerated. Nonetheless, a broad particle size distribution of this nanocomposite ensues from 24 to 37 nm as illustrated in Figure 6c; the average particle size is about 31 nm.

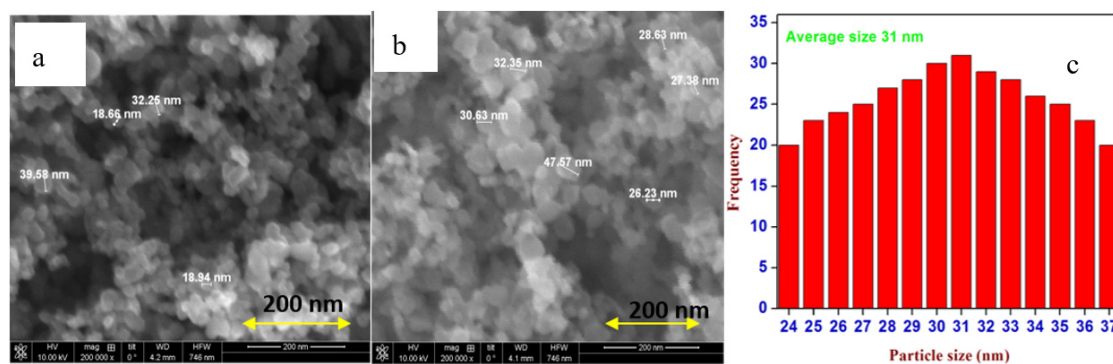


Figure 6. SEM image of (a) TiO_2 and (b) p-C/ TiO_2 , respectively, and (c) particle size distribution of the nanosized p-C/ TiO_2 .

2.2. Photoactivities

2.2.1. Degradation of MB and RhB Dyes under UV Irradiation

To assess the respective photocatalytic activity of p-C/ TiO_2 and of pristine P25 titania specimens, we carried out competitive experiments with two different dyes: MB (Figure 7) and RhB (Figure 8). Dye solutions and the photocatalyst (1 mg mL^{-1}) were mixed and thereafter stirred in the dark for 10 min to allow the adsorption process to reach equilibrium under air-equilibrated conditions.

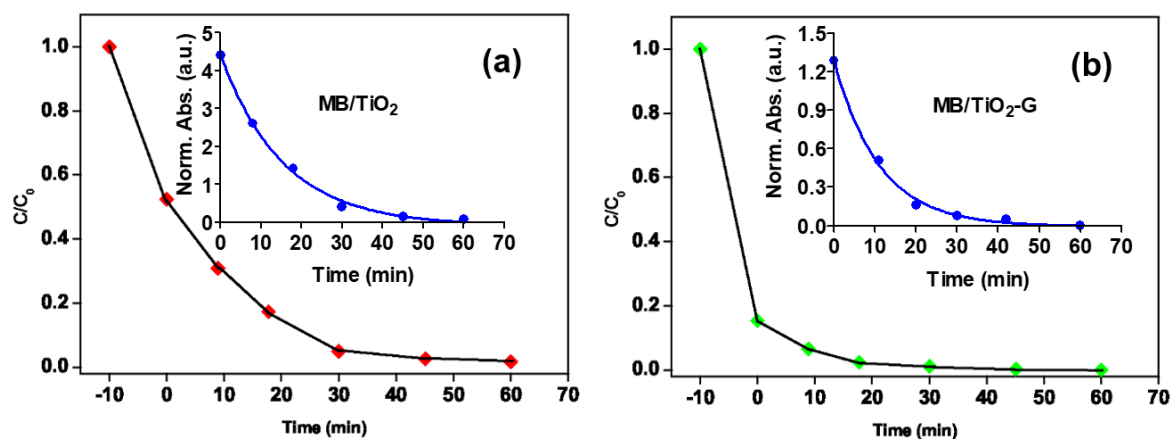


Figure 7. (a) Plot of C/C_0 for the degradation of methylene blue (MB) dye in the presence of TiO_2 with different time intervals at UV light. (b) The same process for the MB/p-C/ TiO_2 suspensions under the same conditions. The region between -10 and 0 min indicates the extent of adsorption of the MB dye by dark conditions. The inserts show the first-order kinetics of the photodegradation of the MB dye.

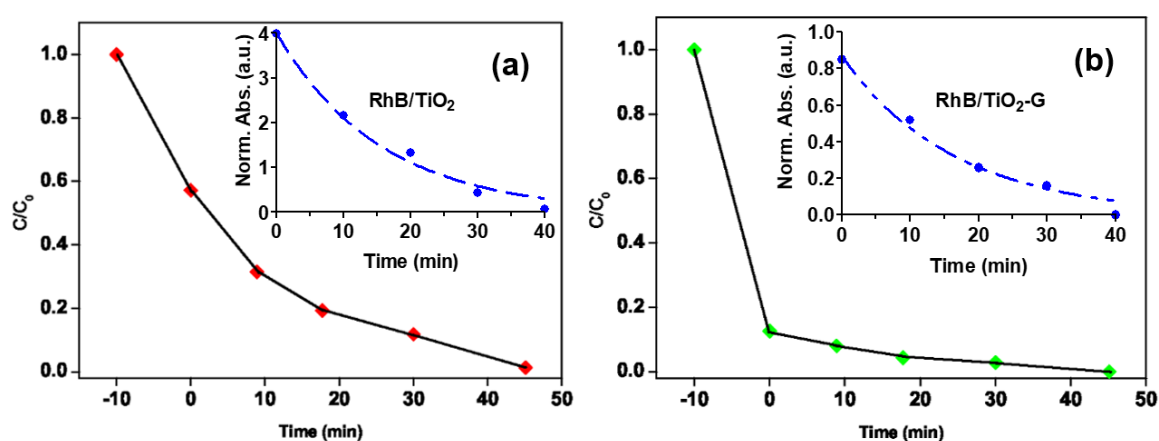


Figure 8. (a) Plot of C/C_0 for the degradation of rhodamine-B (RhB) dye in the presence of TiO₂ with different time intervals at UV light and (b) during the same process for the RhB/p-C/TiO₂ suspensions under identical conditions. The region between −10 and 0 min implies the adsorption of the RhB dye under dark conditions. The inserts show the photodegradation of the RhB dye by first-order kinetics.

As expected, the p-C/TiO₂ samples displayed greater adsorption of the dyes compared to pristine titania (from −10 to 0 min in Figures 7 and 8, respectively, for MB and RhB). Samples were then irradiated at 366 nm with UV lamps; the initial concentrations of the dyes were 1 μ M. The degradations were followed by UV-visible spectroscopy. The inserts in Figures 7 and 8 display the first-order kinetics of the photodegradation of the two dyes. The extent of adsorption of the two dyes on pristine TiO₂ and p-C/TiO₂ specimens together with their respective kinetics are summarized in Table 1.

Table 1. Degree of adsorption and first-order kinetics of photodegradation of dyes MB and RhB having a concentration of 1.0 μ M on pristine TiO₂ and on p-C/TiO₂ in aqueous media under ambient conditions by UV irradiation at 366 nm.

Dye	k (min ^{−1})		% Adsorption in the Dark	
	TiO ₂	p-C/TiO ₂	TiO ₂	p-C/TiO ₂
MB	0.047 ± 0.005	0.091 ± 0.008	48	85
RhB	0.064 ± 0.005	0.060 ± 0.007	43	88

In the absence of light, p-C/TiO₂ absorbs nearly twofold dye with respect to pristine TiO₂ (dark region between −10 and 0 min in Figures 7 and 8; extent of adsorption is reported in Table 1). The enhanced adsorption of dyes on the p-C/TiO₂ system relative to neat TiO₂ is largely the result of the adsorption of the aromatic dyes on the carbon content of the former. Specifically, the physisorption is driven by the π - π^* stacking between the dyes and the aromatic regions of pyrolytic carbon available in the p-C/TiO₂ system. Moreover, because pyrolytic carbon presents high electron mobility, it diminishes electron–hole pair recombination so that the photocatalytic activity of the titania semiconductor in the p-C/TiO₂ nanocomposite should be enhanced [25]. The latter expectation was observed upon UV irradiation of MB in p-C/TiO₂ suspensions that showed the rate of decomposition of MB being twofold faster in the presence of p-C/TiO₂ (0.091 min^{−1}) than with pristine TiO₂ (0.047 min^{−1}).

In the case of RhB, the same trend in adsorption is observed both for neat TiO₂ and p-C/TiO₂. However, unlike the MB case, the kinetics of the degradation are identical within experimental error (Table 1), as evidenced by UV-visible absorption spectroscopy (0.064 min^{−1} versus 0.060 min^{−1}, respectively).

Whenever dyes are used to assess the photoactivities of potential semiconductor photocatalysts using UV-visible light irradiation, it is important to note that such dyes as methylene blue and rhodamine-B (among others) absorb significantly light causing them to act as photosensitizers via

electron injection for their respective excited states onto the conduction band of the photocatalysts (or in some cases also into an intragap defect), which causes them to undergo self-inflicted oxidative degradation through an entirely different mechanistic pathway from the pathway that sees the semiconductor photocatalysts being activated by UV irradiation [23].

Figure 9 summarizes some of the events occurring when UV light is used to activate the TiO₂ or p-C/TiO₂ systems: electron–hole pairs are photogenerated (Equation (1)) following which separation of the charge carriers takes place in competition with recombination (Equation (2)) by migration of the conduction band electrons onto the carbon layer in p-C/TiO₂ (Equation (3)) as a result of its more positive Fermi level [41]. In this regard, while the work function of the carbon layer in graphene is −4.42 eV, the corresponding level of the conduction band of TiO₂ occurs at −4.20 eV [41,42]. Accordingly, the carbon layer in p-C/TiO₂ becomes a scavenger of the TiO₂'s photogenerated electrons aided by the presence of molecular oxygen on the TiO₂ nanoparticles and on the carbon layer to yield the superoxide radical anion O₂•[−] (Equations (4) and (5)), thereby further facilitating charge carrier separation and diminishing electron–hole recombination. Subsequently or concomitantly, the dye undergoes oxidative degradation either directly (Equation (6)) and/or by photogenerated •OH radicals (Equation (8)) (or equivalent reactive oxygen species) produced by valence band holes oxidation of H₂O/OH[−] (Equation (7)). All these events are expected to increase the photocatalytic activity of the TiO₂/p-C/TiO₂ nanocomposite as revealed for the MB dye (twofold increase) but for some elusive reason not for the RhB dye (Table 1).

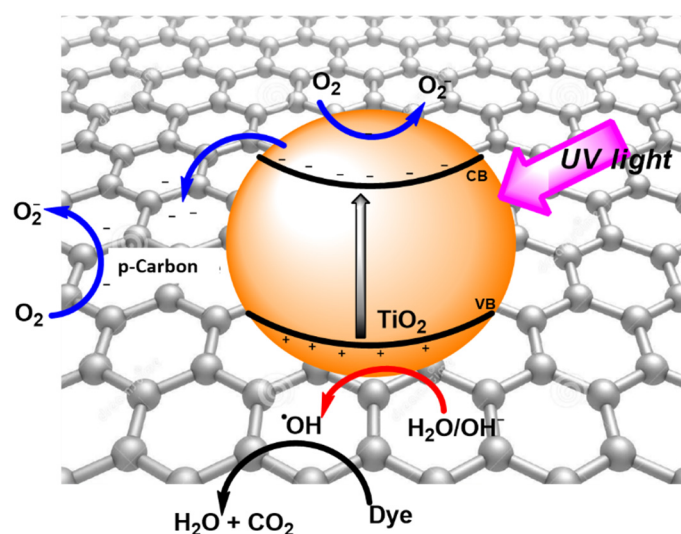
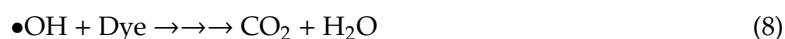
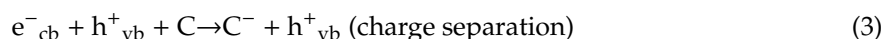
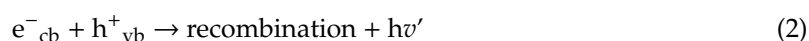


Figure 9. Schematic representation of the activity of the p-C/TiO₂ photocatalyst on dyes.

2.2.2. Photodegradation of Phenol in the Absence and Presence of O₂

To have a better understanding of the photoactivity of p-C/TiO₂ versus pristine TiO₂, the photocatalyzed degradation of phenol was examined using a photoreactor equipped with an immersion UV irradiation lamp (Figure 10a) under both an inert argon atmosphere and in the presence of oxygen. Removal of oxygen was achieved by bubbling argon gas for at least 30 min prior to irradiation; the argon gas flow was maintained throughout the course of the reaction. For the reaction in the presence of oxygen, pure oxygen gas was bubbled throughout the process.

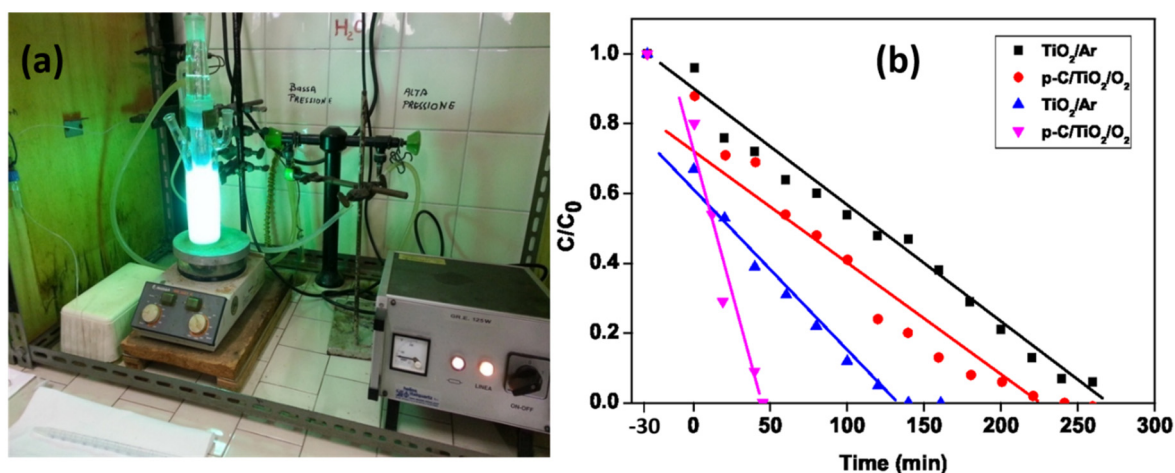


Figure 10. (a) Experimental setup for the photodegradation of phenol; (b) zero-order decrease in the concentration of phenol (1.0 mM, pH 3) in the absence and presence of oxygen under UV irradiation.

Loss of phenol at various time intervals was ascertained by HPLC–UV. Results of the photocatalyzed degradation of this aromatic substrate in the absence and presence of molecular oxygen for pristine TiO₂ and p-C/TiO₂ are illustrated in Figure 10b. The zero-order kinetics of this transformation are summarized in Table 2, which also reports the extent to which the phenol substrate was adsorbed onto pristine TiO₂ and p-C/TiO₂ with and without the presence of oxygen; the data show that the extent of adsorption followed the order TiO₂ (Ar) < p-C/TiO₂ (Ar) < TiO₂ (O₂) < p-C/TiO₂ (O₂). Evidently, both carbon content in p-C/TiO₂ and oxygen impacted significantly on the adsorption of phenol onto the surfaces.

Table 2. Extent of adsorption and initial rates of photodegradation of phenol (1.0 mM; pH 3.0) on pristine TiO₂ and on p-C/TiO₂ in aqueous media under an inert atmosphere (Ar) and in the presence of O₂ exposed to UV irradiation.

Item	TiO ₂ (Ar)	TiO ₂ (O ₂)	p-C/TiO ₂ (Ar)	p-C/TiO ₂ (O ₂)
R_{ini} (10 ^{−3} mM min ^{−1})	3.3 ± 0.1	17.6 ± 0.5	3.5 ± 0.2	4.3 ± 0.3
% adsorption (60 min dark)	3	20	11	32

On the other hand, under the inert argon atmosphere, the presence of carbon in the p-C/TiO₂ system appears to have had no influence on the initial rates of the photoconversion of phenol relative to pristine TiO₂. By contrast, in the presence of molecular oxygen, the initial rate of phenol degradation with p-C/TiO₂ relative to TiO₂ was retarded significantly, with the initial rate being nearly fourfold slower (Table 2). With pristine TiO₂ as the photocatalyst, the initial rate of conversion of phenol was 5.3-fold faster when oxygen was present, but it was only 1.2-fold faster for the p-C/TiO₂ nanocomposite.

Clearly, although the carbon support for the TiO₂ nanoparticles in p-C/TiO₂ is advantageous in depleting the quantity of phenol from aqueous media in the dark, its presence for the

photodegradation process presents little or no advantages in the elimination of phenol photocatalytically. Moreover, the negative influence of a layer of pyrolytic carbon onto TiO_2 nanoparticles on the kinetics of photodegradation of phenol in the presence of oxygen may also arise as a result of oxygen being adsorbed on pyrolytic carbon that causes changes in the electronic nature of pyrolytic carbon in p-C/ TiO_2 . In the past report, namely the “bandgap” of graphene increases from ca. 0.2 eV to as much as 0.45 eV as the oxygen–carbon ratio changes from 0 to ca. 0.08 causing the π^* Fermi surface of graphene to shrink and ultimately vanish [43]. Hopefully, the results obtained here in the presence of molecular oxygen influence in p-C/ TiO_2 catalytic system which may shrink the availability of the carbon layer catalytic function by reaction with molecular oxygen [36].

2.2.3. Photodegradation of Enrofloxacin in Tap Water under Simulated Solar Light

The catalyst p-C/ TiO_2 was also tested for the degradation of ENR, an important rising water pollutant belonging to the class of fluoroquinolone antibiotics. To better appreciate p-C/ TiO_2 efficiency, a further experiment was carried out by employing P25 TiO_2 , the most used and efficient photocatalyst in advanced oxidation processes for environmental remediation.

Before irradiation, 100 mL tap water samples from the municipal waterworks of Pavia (pH 7.7, conductivity at 20 °C: 271 $\mu\text{S cm}^{-1}$), spiked with 10 mg L^{-1} ENR, were sonicated (15 min) in the dark in the presence of 500 mg L^{-1} of each catalyst. Under these conditions, a significant percentage of ENR was adsorbed onto the catalysts, 74% on p-C/ TiO_2 and 43% on P25 TiO_2 . Then, the suspension was irradiated under simulated solar light.

Kinetic experimental data were successfully fitted by a mono-exponential first-order law, using dedicated software (Fig.P application, Fig.P Software Corporation). The degradation profiles, shown in Figure 11, demonstrate that the drug was quantitatively degraded (95%) in less than an hour and a half in presence of both catalysts. Although there is a significant difference between the two kinetic constants (0.030(1) for p-C/ TiO_2 and 0.92(3) for P25 TiO_2), the p-C/ TiO_2 photocatalyst is as efficient as P25 TiO_2 if compared with ENR direct photolysis [44].

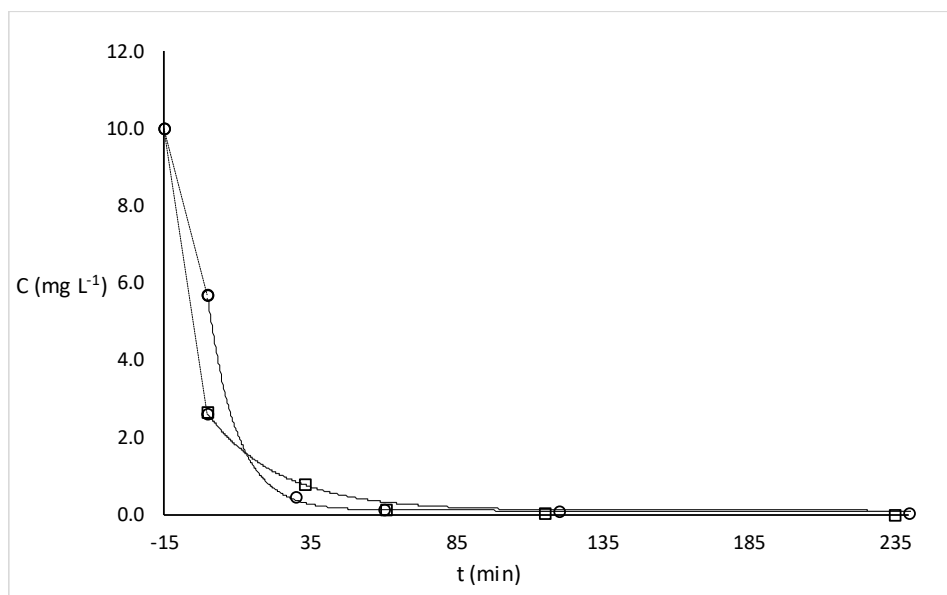


Figure 11. Degradation profiles of enrofloxacin (ENR) (10 mg L^{-1} , tap water) solution obtained under simulated solar light in presence of 500 mg L^{-1} p-C/ TiO_2 (empty square) and Evonik P25 (empty circle).

3. Experimental

3.1. Materials

Evonik P25 titanium dioxide (average particle size: 10–50 nm; specific surface area: 60.8 m²g^{−1}; 77.1% anatase, 15.9% rutile and 7% amorphous) was from Evonik Industries AG (Hanau, Germany). Analytical grade enrofloxacin was provided by Sigma Aldrich (Milan, Italy). Kraft lignin was obtained from Aldrich; with low sulfur content and total sulfur content was 2.89 wt.% (by elemental analysis). Average molecular weight was 10,000 Da. The lignin was water-soluble yielding an alkaline solution. The presence of inorganic sulfate ions was 1.3 wt.%, while the ash content at 600 °C was 17% with respect to dry lignin. The quantity of sulfate in ash was 44 wt.%. Titration with a standard HCl solution showed an equivalent point at 0.026 meq of H⁺ ions for 100 mg of lignin [35]. Characterization of the lignin is available elsewhere [13,19]. All other reagents were of analytical grade and water was doubly distilled over alkaline potassium permanganate using an all-glass apparatus.

3.2. High-Vacuum Pyrolysis of Lignin/TiO₂

A 34 mL volume of kraft lignin aqueous solution (3.25 g L^{−1}) was mixed with the P25 TiO₂ powder (1 g), after which the suspension was stirred for 30 min followed by evaporation of the solvent under vacuum at ambient temperature using a rotary evaporator. This resulted in a thin layer of lignin deposited on the TiO₂ particles' surface, which was then pyrolyzed in a combustion boat under vacuum at 600 °C for 60 min at a rate of 10 °C per min by the following procedure: 100–200 mg of the samples were placed in an alumina combustion boat located inside a quartz tube that was then placed in a cylindrical oven (Watlow ceramic fiber heater, length 305 mm, i.d. 38 mm, electrical power 600 W) and evacuated (10^{−3} Pa) using a double-stage diffusion-rotary vacuum pump. The heating frequency of the oven was 600 °C h^{−1} and the final temperature, i.e., 600 °C, was retained for 20 min. Several pyrolysis temperatures range from 600 to 1200 °C were explored; however, above 600 °C, the anatase phase of TiO₂ converted into the rutile phase. Accordingly, specimens obtained above this temperature were precluded from any subsequent experiments. Each pyrolysis was repeated at least 3 times to evaluate the reproducibility of the experiments.

3.3. Characterization of the Materials

Raman spectra were recorded on the Horiba Jobin-Yvon Labram HR micro-Raman setup having 1 cm^{−1} spectral resolution and a 100× objective (laser spot <1 µm); the laser excitation wavelength was 632.8 nm and power on the sample was <1 mW.

EPR were recorded using the Bruker EMX X-band continuous wave spectrometer furnished with a Bruker ER4119HS EPR cavity. Measurements at differential temperatures were performed by using the Bruker kit.

TGA was carried out under an inert nitrogen atmosphere using the Mettler Toledo TGA1 XP1 apparatus. Samples of 8 to 10 mg were incorporated in an alumina crucible with a perforated lid. A control blank was also performed as well as the empty crucible being detracted from the TGA curves. The heating rate was 10 °C min^{−1} with the gas flow rate was 4 L h^{−1}. For the inert atmospheric conditions, nitrogen gas (<20 ppb of oxygen) was obtained from a gas cylinder with an internal built-in purifier Sapiro BIP filter; samples were purged with nitrogen gas for at least 30 min prior to the start of the TGA analyses. By contrast, TGA carried out under otherwise air-equilibrated conditions used an oil-free membrane pump equipped with a pulsation damper and a condensate drain.

XPS analyses were carried out using a Kratos Axis Ultra DLD spectrometer (Kratos Analytical Ltd., Manchester, UK) equipped with a monochromatic Al K α source ($h\nu = 1486.6$ eV); it was operated at 20 mA and 15 kV. The assessments were carried out on a 300 µm × 700 µm area. Wide scans were collected at a pass energy of 160 eV and energy steps of 1 eV, while high-resolution XPS spectra were recorded at a pass energy of 20 eV and energy steps of 0.1 eV. The Kratos charge neutralizer system was applied for each measurement. Spectra were examined with the Casa XPS software (Casa

Software, Ltd., Teignmouth, UK, version 2.3.17, 2014). SEM analyses were executed by a Zeiss EVO MA10 instrument (Carl Zeiss, Oberkochen, Germany).

3.4. Degradation Procedures and Analyses

UV irradiation was carried out on previously mechanically stirred (10 min in the dark) 100-mL air-equilibrated suspensions of MB or RhB containing 100 mg of neat TiO₂ or p-C/TiO₂ nanocomposite in quartz cylindrical reactors (90 mm diameter × 25 mm height); initial concentrations of the dyes were 1.0 µM. The UV light source consisted of two 15-W phosphor-coated lamps (center of emission, 366 nm). Four-milliliter aliquots were withdrawn at 5-min intervals during the irradiation, and after removal of the solids were immediately measured by UV-visible absorption spectroscopy in 1-cm quartz cuvettes using either a JASCO V-630 UV-visible spectrophotometer or a Cary 19 instrument.

UV irradiation of TiO₂ and p-C/TiO₂ dispersions in phenol solutions was achieved using an immersion-lamp reactor equipped with 250-W Hg medium pressure lamp as the light source; the initial concentration of phenol was 1.0 mM in aqueous media at a pH of 3.0 (adjusted by HNO₃). A water circulating cooling system provided control of the temperature of the reactor during irradiation; temperature was kept at 20 ± 1 °C. A Pyrex water bath was also positioned between the reactor and the light source to filter out IR radiation. Except for dark adsorption determination, air equilibration was achieved by purging the dispersions with air during irradiation. On the other hand, except for dark adsorption determination, the dispersions were continually purged with argon gas during irradiation. The reactor material (silicate glass) excluded wavelengths shorter than 320 nm from the cell. At specified times (5-min intervals for each measurement), 1.0 mL aliquots of the samples were withdrawn and immediately injected into the HPLC–UV system for analysis. The C18 column mobile phase was H₂O/acetonitrile (80:20) at a flow rate of 1 mL min^{−1}.

For enrofloxacin (ENR) degradation, the suspension (500 mg L^{−1} catalyst) was irradiated in a closed glass container (40 mm depth, exposed surface 9500 mm²) by employing a Solar Box 1500e (CO.FO.ME.GRA S.r.l., Milan, Italy) set at a power aspect of 250 W m^{−2}, and supplied with UV outdoor filter produced of IR-treated soda lime glass. Replicated photoproduction experiments were done on all samples. During irradiation, aliquots (1 mL) of each sample were withdrawn at the specific times, filtered (0.2 µm nylon filter) and injected in the HPLC–UV system (LC-20AT solvent delivery module equipped with a DGU-20A3 degasser and interfaced with an SPD-20A UV detector (Shimadzu, Milan, Italy). The analysis wavelength chosen was 275 nm. Twenty microliters of each sample were introduced into a 250 × 4.6 mm, 5 µm Analytical Ascentis C18 (Supelco, Sigma Aldrich Corporation, Milan, Italy) combined with a related guard column. The mobile phase was 25 mM H₃PO₄/acetonitrile (85:15), at a flow speed of 1 mL min^{−1}.

4. Concluding Remarks

This study has shown that titania can be coated successfully with pyrolytic carbon starting from inexpensive waste material such as kraft lignin. The pyrolytic process performed at 600 °C did not affect the crystalline state of the P25 TiO₂ photocatalyst as evidenced by XRD, XPS, EPR, TGA and Raman spectral analyses. The carbonaceous titania obtained from the pyrolysis was identified and deposited onto the metal oxide surface, whose photocatalytic activity was measured against pristine P25 TiO₂ by evaluation of the kinetics of degradation of RhB and MB, phenol and ENR under UV irradiation (both in the presence and absence of oxygen) and simulated solar light, respectively. Results evidenced how the as-prepared p-C/TiO₂ photocatalyst performed better as an adsorbent of the two dyes (by a factor of two). Under UV light irradiation, the first-order kinetics of degradation were twofold greater for the MB dye but otherwise identical for the RhB dye. In this regard, the use of dyes in assessing photocatalytic activity of photocatalysts under UV irradiation and under visible or UV-visible irradiation has been discussed and it is argued that dyes should not be used whenever visible light is used because the dyes can act as photosensitizers of the semiconductor photocatalyst through electron injection from their excited states thereby inflicting their own degradation. Accordingly, a comparative study of the photodegradation of

phenol was performed with pristine TiO₂ and p-C/TiO₂ nanocomposite samples under UV irradiation and with/without molecular oxygen to alleviate this issue. Results showed that both pristine TiO₂ and p-C/TiO₂ systems are better adsorbents under oxygenated conditions vis-a-vis inert conditions, and that under UV irradiation the zero-order rate for pristine TiO₂ was significantly faster in the presence of oxygen, but only slightly faster for the p-C/TiO₂ system. Finally, the photocatalytic performance of p-C/TiO₂ was assessed for the degradation of a fluoroquinolone antibiotic in tap water under simulated sunlight. Overall, p-C/TiO₂ showed higher adsorption properties and a smaller/equal photocatalytic efficiency compared to P25 TiO₂. Contrary to previous reports [29,30], we conclude that although the presence of the carbon layer enhances the adsorption of substrates onto the p-C/TiO₂ photocatalyst, the carbon layer inhibits somewhat the degradation process as the pyrolytic carbon layer hampers the organic substrates from interacting directly with the oxidizing entities photogenerated on the UV light-activated metal oxide photocatalyst. However, the high adsorption capacity in the dark could be a method to simultaneously concentrate and photodegrade pollutants present in small amounts in water samples.

Author Contributions: Conceptualization, D.D.; methodology, D.D.; software, D.S.B.; validation, D.V., I.M. and D.D.; formal analysis, V.B.; investigation, D.V.; data curation, A.S., V.B., M.S.; writing—original draft preparation, D.V., M.S.; writing—review and editing, D.D., A.S.; supervision, D.D. All authors have read and agreed to the published version of the manuscript.

Funding: This research received no external funding.

Acknowledgments: We are grateful to the PANACEA–ERASMUS MUNDUS of the European Commission within the project Agreement Number 2012-2647/001-001-EMA2 for an Action 2 scholarship in support of Dhanalakshmi Vadivel. Nick Serpone of the Photo Green Laboratory of the Department of Chemistry at the University of Pavia for useful discussions. This research was funded by the Spanish Ministry of Economy and Competitiveness, project MAT2016-75955-C2-2-R.

Conflicts of Interest: The authors declare no conflict of interest.

References

1. Yuan, J.; Zhou, S.; Wu, L.; You, B. Organic pigment particles coated with titania via sol–gel process. *J. Phys. Chem. B* **2006**, *110*, 388–394. [[CrossRef](#)]
2. Ohko, Y.; Tatsuma, T.; Fujii, T.; Naoi, K.; Niwa, C.; Kubota, Y.; Fujishima, A. Multicolour photochromism of TiO₂ films loaded with silver nanoparticles. *Nat. Mater.* **2002**, *2*, 29–31. [[CrossRef](#)]
3. Lee, S.; Cho, I.-S.; Lee, J.H.; Kim, D.H.; Kim, D.W.; Kim, J.Y.; Shin, H.; Lee, J.-K.; Jung, H.S.; Park, N.-G. Two-step sol–gel method-based TiO₂ nanoparticles with uniform morphology and size for efficient photo-energy conversion devices. *Chem. Mater.* **2010**, *22*, 1958–1965. [[CrossRef](#)]
4. Bao, S.J.; Li, C.M.; Zang, J.F.; Cui, X.Q.; Qiao, Y.; Guo, J. New nanostructured TiO₂ for direct electrochemistry and glucose sensor applications. *Adv. Funct. Mater.* **2008**, *18*, 591–599. [[CrossRef](#)]
5. Yu, J.; Wang, W.; Cheng, B.; Su, B.-L. Enhancement of photocatalytic activity of mesoporous TiO₂ powders by hydrothermal surface fluorination treatment. *J. Phys. Chem. C* **2009**, *113*, 6743–6750. [[CrossRef](#)]
6. Rothenberger, G.; Moser, J.; Gratzel, M.; Serpone, N.; Sharma, D.K. Charge Carrier Trapping and Recombination Dynamics in Small Semiconductor Particles. *J. Am. Chem. Soc.* **1985**, *107*, 8054–8059. [[CrossRef](#)]
7. Hu, X.; Li, G.; Yu, J.C. Design, fabrication, and modification of nanostructured semiconductor materials for environmental and energy applications. *Langmuir* **2009**, *26*, 3031–3039. [[CrossRef](#)] [[PubMed](#)]
8. Kumar, S.G.; Devi, L.G. Review on modified TiO₂ photocatalysis under UV/visible light: Selected results and related mechanisms on interfacial charge carrier transfer dynamics. *J. Phys. Chem. A* **2011**, *115*, 13211–13241. [[CrossRef](#)] [[PubMed](#)]
9. Zhang, J.; Wu, Y.; Xing, M.; Leghari, S.A.K.; Sajjad, S. Development of modified N- doped TiO₂ photocatalyst with metals, nonmetals and metal oxides. *Energy Environ. Sci.* **2010**, *3*, 715–726. [[CrossRef](#)]
10. Wu, G.; Wang, J.; Thomas, D.F.; Chen, A. Synthesis of F-doped flower-like TiO₂ nanostructures with high photoelectrochemical activity. *Langmuir* **2008**, *24*, 3503–3509. [[CrossRef](#)] [[PubMed](#)]

11. Zhuang, J.; Tian, Q.; Zhou, H.; Liu, Q.; Liu, P.; Zhong, H. Hierarchical porous TiO₂@C hollow microspheres: One-pot synthesis and enhanced visible-light photocatalysis. *J. Mater. Chem.* **2012**, *22*, 7036–7042. [[CrossRef](#)]
12. Woan, K.; Pyrgiotakis, G.; Sigmund, W. Photocatalytic carbon-nanotube–TiO₂ composites. *Adv. Mater.* **2009**, *21*, 2233–2239. [[CrossRef](#)]
13. Nor, N.M.; Chung, L.L.; Teong, L.K.; Mohamed, A.R. Synthesis of activated carbon from lignocellulosic biomass and its applications in air pollution control—A review. *J. Environ. Chem. Eng.* **2013**, *1*, 658–666.
14. Farhangi, N.; Medina-Gonzalez, Y.; Chowdhury, R.R.; Charpentier, P.A. Growing TiO₂ nanowires on the surface of graphene sheets in supercritical CO₂: Characterization and photo efficiency. *Nanotechnology* **2012**, *23*, 294005. [[CrossRef](#)] [[PubMed](#)]
15. Xiang, Q.; Yu, J.; Jaroniec, M. Graphene-based semiconductor photocatalysts. *Chem. Soc. Rev.* **2012**, *41*, 782–796. [[CrossRef](#)]
16. Liu, B.; Huang, Y.; Wen, Y.; Du, L.; Zeng, W.; Shi, Y.; Zhang, F.; Zhu, G.; Xu, X.; Wang, Y. Highly dispersive f001g facets-exposed nanocrystalline TiO₂ on high quality graphene as a high performance photocatalyst. *J. Mater. Chem.* **2012**, *22*, 7484–7491. [[CrossRef](#)]
17. Wang, W.-S.; Wang, D.-H.; Qu, W.-G.; Lu, L.-Q.; Xu, A.-W. Large ultrathin anatase TiO₂ nanosheets with exposed f001g facets on graphene for enhanced visible light photocatalytic activity. *J. Phys. Chem. C* **2012**, *116*, 19893–19901. [[CrossRef](#)]
18. Geim, A.K.; Novoselov, K.S. The rise of graphene. *Nat. Mater.* **2007**, *6*, 183–191. [[CrossRef](#)]
19. Suhas, M.; Carrott, P.J.; Ribeiro Carrott, M.M.L. Lignin—From natural adsorbent to activated carbon: A review. *Biores. Technol.* **2007**, *98*, 2301–2312. [[CrossRef](#)]
20. Fierro, V.; Torne-Fernandez, V.; Celzard, A. Kraft lignin as a precursor for microporous activated carbons prepared by impregnation with ortho-phosphoric acid: Synthesis and textural characterisation. *Microporous Mesoporous Mater.* **2006**, *92*, 243–250. [[CrossRef](#)]
21. Gu, L.; Zhang, H.; Jiao, Z.; Li, M.; Wu, M.; Lei, Y. Glucosamine-induced growth of highly distributed TiO₂ nanoparticles on graphene nanosheets as high-performance photocatalysts. *RSC Adv.* **2016**, *6*, 67039–67048. [[CrossRef](#)]
22. Sun, M.; Li, W.; Sun, S.; He, J.; Zhang, Q.; Shi, Y. One-step in situ synthesis of graphene-TiO₂ nanorod hybrid composites with enhanced photocatalytic activity. *Mater. Res. Bull.* **2015**, *61*, 280–286. [[CrossRef](#)]
23. Wu, T.; Liu, G.; Zhao, J.; Hidaka, H.; Serpone, N. Photo assisted degradation of dye pollutants. V. Self-photosensitized oxidative transformation of rhodamine-B under visible light irradiation in aqueous TiO₂ dispersions. *J. Phys. Chem. B* **1998**, *102*, 5845–5851. [[CrossRef](#)]
24. Dong, P.; Wang, Y.; Guo, L.; Liu, B.; Xin, S.; Zhang, J.; Shi, Y.; Zeng, W.; Yin, S. A facile one-step solvothermal synthesis of graphene/rod-shaped TiO₂ nanocomposite and its improved photocatalytic activity. *Nanoscale* **2012**, *4*, 4641–4649. [[CrossRef](#)]
25. Giovannetti, R.; Rommozzi, E.; Zannotti, M.; D’Amato, C.A. Recent advances in graphene-based TiO₂ nanocomposites (GTiO₂Ns) for photocatalytic degradation of synthetic dyes. *Catalysts* **2017**, *7*, 305. [[CrossRef](#)]
26. Jiang, G.; Lin, Z.; Chen, C.; Zhu, L.; Chang, Q.; Wang, N.; Wei, W.; Tang, H. TiO₂ nanoparticles assembled on GO nanosheets with high photocatalytic activity for removal of pollutants. *Carbon* **2011**, *49*, 2693–2701. [[CrossRef](#)]
27. Gao, Y.; Pu, X.; Zhang, D.; Ding, G.; Shao, X.; Ma, J. Combustion synthesis of GO–TiO₂ hybrid materials for photodegradation of methyl orange. *Carbon* **2012**, *49*, 4093–4101. [[CrossRef](#)]
28. Sun, L.; Zhao, Z.; Zhou, Y.; Liu, L. Anatase TiO₂ nanocrystals with exposed f001g facets on graphene sheets via molecular grafting for enhanced photocatalytic activity. *Nanoscale* **2012**, *4*, 613–620. [[CrossRef](#)]
29. Zhang, H.; Lv, X.; Li, Y.; Wang, Y.; Li, J. P25-Graphene Composite as a High Performance Photocatalyst. *ACS Nano* **2010**, *4*, 380–386. [[CrossRef](#)]
30. Du, J.; Lai, X.; Yang, N.; Zhai, J.; Kisailus, D.; Su, F.; Wang, D.; Jiang, L. Hierarchically Ordered Macro-Mesoporous TiO₂-Graphene Composite Films: Improved Mass Transfer, Reduced Charge Recombination, and Their Enhanced Photocatalytic Activities. *ACS Nano* **2011**, *5*, 590–596. [[CrossRef](#)]
31. Wang, X.; Zhang, J.; Zhang, X.; Zhu, Y. Characterization, uniformity and photocatalytic properties of graphene/TiO₂ nanocomposites via Raman mapping. *Optics Express* **2017**, *25*, 21496. [[CrossRef](#)] [[PubMed](#)]
32. Posa, V.R.; Annavaram, V.; Koduru, J.R.; Bobbala, P.; Somala, M.V.; Somala, A.R. Preparation of graphene–TiO₂ nanocomposite and photocatalytic degradation of Rhodamine-B under solar light irradiation. *J. Experim. Nanosci.* **2016**, *11*, 722–736. [[CrossRef](#)]

33. Martins, P.M.; Ferreira, C.G.; Silva, A.R.; Magalhães, B.; Alves, M.M.; Pereira, L.; Marques, P.A.A.P.; Melle-Franco, M.; Lanceros-Méndez, S. TiO₂/graphene and TiO₂/graphene oxide nanocomposites for photocatalytic applications: A computer modeling and experimental study. *Compos. Part B* **2018**, *145*, 39–46. [[CrossRef](#)]
34. Zhang, Q.; Bao, N.; Wang, X.; Hu, X.; Miao, X.; Chaker, M.; Ma, D. Advanced fabrication of chemically bonded graphene/TiO₂ continuous fibers with enhanced broadband photocatalytic properties and involved mechanisms exploration. *Sci. Rep.* **2016**, *6*, 38066. [[CrossRef](#)] [[PubMed](#)]
35. Dondi, D.; Zeffiro, A.; Speltini, A.; Tomasi, C.; Vadivel, D.; Buttafava, A. The role of inorganic sulfur compounds in the pyrolysis of Kraft lignin. *J. Anal. Appl. Pyrol.* **2014**, *107*, 53–58. [[CrossRef](#)]
36. Vadivel, D.; Speltini, A.; Zeffiro, A.; Bellani, V.; Pezzini, S.; Buttafava, A.; Dondi, D. Reactive carbons from Kraft lignin pyrolysis: Stabilization of peroxy radicals at carbon/silica interface. *J. Anal. Appl. Pyrol.* **2017**, *128*, 346–352. [[CrossRef](#)]
37. Qiu, B.; Zhou, Y.; Ma, Y.; Yang, X.; Sheng, W.; Xing, M.; Zhang, J. Facile synthesis of the Ti³⁺ self-doped TiO₂-graphene nanosheet composites with enhanced photocatalysis. *Sci. Rep.* **2015**, *5*, 8591. [[CrossRef](#)]
38. Lyon, T.J.; Sichau, J.; Dorn, A.; Centeno, A.; Pesquera, A.; Zurutuza, A.; Blick, R.H. Probing Electron Spin Resonance in Monolayer Graphene. *Phys. Rev. Lett.* **2017**, *119*, 066802. [[CrossRef](#)]
39. Panich, A.M.; Shames, A.I.; Tsindlekht, M.I.; Yu, V.; Osipov, V.; Patel, M.; Savaram, K.; He, H. Structure and magnetic properties of pristine and Fe-doped micro- and nano-graphenes. *J. Phys. Chem. C* **2016**, *120*, 3042–3053. [[CrossRef](#)]
40. Yasse, A.S.; Shahed, U.M. Khan Visible light active carbon modified n-TiO₂ for efficient hydrogen production by photoelectrochemical splitting of water. *Int. J. Hydrogen Energy* **2008**, *33*, 1118–1126.
41. Guoxin, H.; Tang, B. Photocatalytic mechanism of graphene/titanate nanotubes photocatalyst under visible-light irradiation. *Mater. Chem. Phys.* **2013**, *138*, 608–614.
42. Cruz, M.; Gomez, C.; Duran-Valle, C.J.; Pastrana-Martínez, L.M.; Faria, J.L.; Silva, A.M.T.; Faraldos, M.; Bahamonde, A. Bare TiO₂ and graphene oxide TiO₂ photocatalysts on the degradation of selected pesticides and influence of the water matrix. *Appl. Surf. Sci.* **2017**, *416*, 1013–1021. [[CrossRef](#)]
43. Takahashi, T.; Sugawara, K.; Noguchi, E.; Sato, T.; Takahashi, T. Band-gap tuning of monolayer graphene by oxygen adsorption. *Carbon* **2014**, *73*, 141–145. [[CrossRef](#)]
44. Sturini, M.; Speltini, A.; Maraschi, F.; Rivaglia, E.; Pretali, L.; Malavasi, L.; Profumo, A.; Fasani, E.; Albini, A. Sunlight photodegradation of marbofloxacin and enrofloxacin adsorbed on clay minerals. *J. Photochem. Photobiol. A* **2015**, *299*, 103–109. [[CrossRef](#)]

